Title

Technique development of 3D dynamic CS-EPSI for hyperpolarized 13C pyruvate MR molecular imaging of human prostate cancer



Journal

Magnetic Resonance in Medicine, 80(5)

ISSN

0740-3194

Authors

Chen, Hsin-Yu

Larson, Peder EZ

Gordon, Jeremy W

et al.

Publication Date

2018-11-01

DOI

10.1002/mrm.27179

Peer reviewed

HHS Public Access

Author manuscript

*Magn Reson Med*. Author manuscript; available in PMC 2019 November 01.

Published in final edited form as:

*Magn Reson Med*. 2018 November ; 80(5): 2062–2072. doi:10.1002/mrm.27179.

# Technique Development of 3D Dynamic CS-EPSI for Hyperpolarized $^{13}$C Pyruvate MR Molecular Imaging of Human Prostate Cancer

**Hsin-Yu Chen**[1], **Peder E.Z. Larson**[1], **Jeremy W. Gordon**[1], **Robert A. Bok**[1], **Marcus Ferrone**[2], **Mark van Criekinge**[1], **Lucas Carvajal**[1], **Peng Cao**[1], **John M. Pauly**[3], **Adam B. Kerr**[3], **Ilwoo Park**[4], **James B. Slater**[1], **Sarah J. Nelson**[1], **Pamela N. Munster**[5], **Rahul Aggarwal**[5], **John Kurhanewicz**[1], and **Daniel B. Vigneron**[1]

[1]Department of Radiology and Biomedical Imaging, University of California, San Francisco

[2]Department of Clinical Pharmacy, University of California, San Francisco

[3]Electrical Engineering, Stanford University, Stanford, California

[4]Department of Radiology, Chonnam National University Medical School and Hospital, Korea

[5]Department of Medicine, University of California, San Francisco

## Abstract

**Purpose—**The purpose of this study was to develop a new 3D dynamic carbon-13 compressed sensing EPSI MR sequence and test it in phantoms, animal models, and then in prostate cancer patients to image the metabolic conversion of hyperpolarized [1-$^{13}$C]pyruvate to [1-$^{13}$C]lactate with whole gland coverage at high spatial and temporal resolution.

**Methods—**A 3D dynamic CS-EPSI sequence with spectral-spatial excitation was designed to meet the required spatial coverage, time and spatial resolution, and RF limitations of the 3T MR scanner for its clinical translation for prostate cancer patient imaging. Following phantom testing, animal studies were performed in rats and transgenic mice with prostate cancers. For patient studies, a GE SPINlab polarizer was used to produce hyperpolarized sterile GMP [1-$^{13}$C]pyruvate. 3D dynamic $^{13}$C CS-EPSI data were acquired starting 5s after injection throughout the gland with a spatial resolution of 0.5cm$^3$, 18 timeframes, 2s temporal resolution, and 36s total acquisition time.

**Results—**Through preclinical testing, the 3D CS-EPSI sequence developed in this project was shown to provide the desired spectral, temporal and spatial 5-dimensional HP $^{13}$C MR data. In human studies, the 3D dynamic HP CS-EPSI approach provided first-ever simultaneously volumetric and dynamic images of the LDH-catalyzed conversion of [1-$^{13}$C]pyruvate to [1-$^{13}$C]lactate in a biopsy-proven prostate cancer patient with full gland coverage.

**Corresponding author:** Hsin-Yu Chen, Department of Radiology and Biomedical Imaging, University of California, San Francisco, 1700 Fourth Street, Byers Hall Suite 102, San Francisco, CA 94158, Hsin-yu.Chen@ucsf.edu, Phone: 415-514-4454, Fax: 415-514-4451.

**Conclusion—**The results demonstrate the feasibility to characterize prostate cancer metabolism in animals and now patients using this new 3D dynamic HP MR technique to measure the kinetic rate constant, $k_{PL}$, of the conversion of [1-$^{13}$C]pyruvate to [1-$^{13}$C]lactate.

### Keywords

Hyperpolarized C-13 pyruvate; 3D dynamic imaging; Human prostate cancer

## 1. Introduction

Hyperpolarized (HP) $^{13}$C MR using dissolution dynamic nuclear polarization (dDNP) has been shown in over 100 published animal studies to provide unprecedented information on previously-inaccessible aspects of biological processes by detecting endogenous, nontoxic $^{13}$C-labeled probes that can monitor enzymatic conversions through key biochemical pathways [1–11]. Also, a human Phase 1 clinical trial using a custom-designed polarizer in a cleanroom demonstrated the safety and feasibility of HP $^{13}$C-pyruvate MRI in prostate cancer patients [12]. This clinical trial indicated the potential to characterize the extent and aggressiveness of prostate cancer in individual subjects to ultimately benefit clinical treatment decisions and to monitor treatment response which is an unmet clinical need [12]. However, the acquisition techniques used in that first human study provided only slice dynamic information on the conversion of [1-$^{13}$C]pyruvate to [1-$^{13}$C]lactate and single time point 3D $^{13}$C MRSI data acquired over 12 seconds. To be clinically useful, dynamic 3D acquisitions with full gland coverage are required and with a spatial resolution fine enough to study 0.5cm$^3$ tumors and a temporal resolution adequate to measure quantitatively the conversion rate, $k_{PL}$, of pyruvate to lactate.

The goal of this project was to develop a new dynamic and volumetric acquisition to detect HP pyruvate uptake and enzymatic conversion throughout the prostate with high spatial and temporal resolution. A new 3D dynamic compressed sensing EPSI (3D dynamic CS-EPSI) sequence was developed and comprised of spectral-spatial RF excitations with multiband and variable-flip schemes, followed by a compressed-sensing EPSI readout using random blip encoding. The 3D dynamic imaging protocol was tested in phantoms, transgenic mice of prostate cancer (TRAMPs) and rats before translating this approach for human studies. The translational challenges, including larger imaging volume, reduced peak RF power and lower B1 inhomogeneity were addressed through the optimization of pulse design and sequence parameters.

## 2. Methods

### Pulse sequences

A 3D dynamic compressed-sensing EPSI (3D CS-EPSI) sequence was designed and optimized to provide more efficient, higher SNR hyperpolarized $^{13}$C MR scans of pyruvate metabolism in animals and humans. The backbone of this sequence consists of a spectral-spatial RF excitation pulse, followed by a compressed sensing EPSI readout. Prior TRAMP studies [1, 13] used a double-spin echo (DSE) refocusing pulse to provide narrow spectral lines and improve SNR (TE/TR = 150/250ms, Fig. 1A). But for patient studies, no spin-echo

refocusing pulses were used (Fig. 1B) due to peak power limitations and the increased B1 inhomogeneity for the clamshell transmit coil. The estimated SAR of the 3D CS-EPSI sequence was well below the FDA requirements. The three-dimensional readout scheme utilized pseudorandom "blip" encoding in the $k_x$-$k_y$-dynamic directions and flyback echo-planar spectral-imaging (EPSI) in the $k_z$-$k_t$ dimensions. The compressed sensing reconstruction takes advantage of the sparsity in the spatial and temporal-wavelet dimensions to recover undersampled k-space locations using L1-minimization with total variation penalty, achieving 18× acceleration. The EPSI readout enabled another 16-fold acceleration compared to conventional chemical-shift imaging by the rapid simultaneous spectral-spatial encoding [14, 15]. A combined 288× acceleration factor condenses a 10-minute fully-sampled MRSI acquisition into a 2-second undersampled time interval. Acquiring data without DSE refocusing pulses required modification of the prior compressed sensing reconstruction algorithm [1, 15] to incorporate spectral phasing and minimize linewidth broadening. The reconstruction included a linear phase correction to account for the additional phase caused by sampling delay.

## RF Pulses Design

The RF excitation pulse provided multiband excitation to account for the metabolic conversions between $^{13}$C pyruvate and lactate. Moreover, a "variable flip angle" scheme was applied, where the excitation flip angle on each metabolite was progressively increased to account for the loss from previous excitations and the intrinsic $T_1$ relaxation. The flip angles were calculated based on a "$T_1$-effective" scheme, ensuring adequate pyruvate signal-to-noise ratio while maximizing total lactate SNR for robust modeling of metabolic conversion and parameter estimation [16]. The spectral-spatial pulses were designed using the SS-RF toolbox developed by Larson et al [17].

A new spectral-spatial RF pulse was designed and generated to account for the limitation on peak power in the clinical setup (Fig.2A). The new SSRF pulse has a peak B1 of 0.597G and duration of 6.3ms, which is a 67% reduction of peak power and 30% reduction in length compared to our preclinical designs (peak B1 = 1.796G, duration = 8.9ms, applied in the preclinical datasets in this study). The pulse bandwidth was 793Hz. The ripple was set to less than 1% in both passband and stopband to ensure reasonably homogeneous pulse profile. The $^{13}$C RF calibration protocol is summarized in the Supplementary Methods.

## 3D Imaging Coverage

The 3D CS-EPSI sequence [15] was designed to offer full 3D coverage for the regions of interest with high spatiotemporal resolution in both preclinical [1] and now clinical research in this study. In TRAMP mice studies, the sequence was configured to cover the entire animal, which has two advantages. First, the coverage allows for blood vessels such as the iliac artery to be included, and therefore enables acquisition of the arterial input function (AIF) and potentially factor perfusion into the dynamic modeling. Secondly, it allows not only imaging the primary tumor, but common metastatic sites, such as peri-arterial(PA) and peri-renal(PR) lymph nodes. In addition, it monitors key physiological regions such as kidney and liver for possible abnormalities associated with prostate cancer. In rat studies, the FOV was chosen to extend through the rat trunk for similar reasoning. In clinical exams, the

sequence covers the full prostate gland from base to apex, including the peripheral, central and transition zones. The 581Hz-spectral bandwidth ensures inclusion of the two main biomarkers in preclinical studies, namely HP-$^{13}$C pyruvate and lactate. Note the urea phantom was spectrally aliased in order to conserve spectral bandwidth for improved SNR efficiency.

## MRI Experiments

Eleven sets of hyperpolarized $^{13}$C dynamic MRSI were acquired on a total of 6 TRAMP mice and 3 healthy rats using the 3D dynamic CS-EPSI. 3 TRAMPs had histologically aggressive late stage, and 3 had early stage tumors in this study. N=8 datasets were collected from TRAMP experiments, with two mice studied twice (on different days) among the cohort of six.

Two mice were studied twice among the cohort of six. [1-$^{13}$C]pyruvate was polarized by a GE SPINlab clinical polarizer (GE Healthcare, Waukesha WI) using the dDNP technique for 2 hours, yielding 25–35% pyruvate polarization. The $^{13}$C substrate was rapidly dissolved and injected into the subject animal through a tail vein catheter. For the TRAMP studies, ~350ul bolus was injected over 15s, whereas the rats received ~3ml bolus over 12s. In both cases, the sequence was initiated at t=15 seconds since the beginning of injection. All studies were performed on a 3T clinical scanner (GE Healthcare, Waukesha WI). The mouse and rat studies were done using custom-built, dual-tuned $^{1}$H and $^{13}$C mouse and rat coils, respectively. Dose per unit weight was approximately 10ml/kg for TRAMP mouse, 6ml/kg for rat, both injected with 80mM solution.

For TRAMP mouse studies, the 3D CS-EPSI sequence was chosen to provide a spatial resolution of 3.3 × 3.3 × 5.4mm, a temporal resolution of 2s, a FOV of 4 × 4 × 8.6cm, a spectral BW of 581Hz, and 18 timeframes in 36 seconds. For rats, the FOV and the spatial voxel size were both doubled to provide larger coverage (spatial resolution = 6.7 × 6.7 × 10.8mm, FOV = 8 × 8 × 17.2cm), whereas temporal resolution and acquisition window remained the same as TRAMP scans. The HP-$^{13}$C voxel volume for mouse and rat scans were 0.059 and 0.480 cm$^3$, respectively. A proton $T_2$-FSE sequence was prescribed for anatomical reference in TRAMP exams, whereas a bSSFP sequence served as the reference in rat studies.

Phantom studies were conducted using the full clinical configuration with clamshell transmit and endorectal receive coils. The phantom setup includes a built-in $^{13}$C-urea phantom positioned on the receive coil (8M, 600ul) and two ethylene glycol phantoms (natural abundance, $^{13}$C concentration=0.17M). The pulse sequence for the clinical studies was used.

For the human study (N=1), GMP-grade sterile [1-$^{13}$C] pyruvic acid with 15mM trityl radical was polarized in Spinlab for ~2 hours, dissolved with sterile water, and subjected to radical filtration, neutralization, and sterile filtration into a Medrad syringe. An automatic post-dissolution QC reported key parameters including pyruvate concentration (253mM), polarization level (37%), radical concentration (0.7uM), pH (7.8) and temperature (32.9°C), and a pharmacist determined that the bolus met all safety standards for injection. Dosage was calculated based on patient weight for 0.43mL/kg of the 250mM sterile pyruvate

solution. The injection used a power injector (Spectris Solaris, Medrad, Saxonburg, PA) at a rate of 5ml/s, followed by flush of saline. Total injection time was around 10–15 seconds depending on patient weight.

In the clinical setup, a clamshell volume coil was used for $^{13}C$ transmit, and a dual-tuned endorectal coil for receive. The resolution for the patient study was as follows (spatial resolution = 8×8×8mm isotropic, FOV = 9.6×9.6×12.8cm). Acquisition window was 36s for the patient study, with voxel volume of $0.5cm^3$. The proton acquisitions were done using a 4-channel pelvic phased coil array in combination with the $^{1}H$-tuned endorectal coil element. A T2-weighted fast-spin echo sequence provided anatomical reference, with the following parameters: FOV 18×18×7.2cm, spatial resolution = 0.35×0.35×3mm, TE/TR =102/5000 ms, NEX = 3.

The human research was conducted with the approval from Institutional Review Board, and all animal studies were conducted in accordance with the policies of Institutional Animal Care and Use Committee at University of California, San Francisco.

## Data Analysis

The hyperpolarized $^{13}C$ 3D CS-EPSI data were reconstructed using an in-house command-line script combined with MATLAB routine [1, 15]. A combination of an open-source SIVIC image processing software [18] and MATLAB was used for examination of the fully-3D spectrum voxel-by-voxel, over a specific slice and orientation, or across a given time frame. Overlay of HP-$^{13}C$ images, image-based statistics or modeled metabolic and perfusion indices such as $k_{PL}$ and $k_{trans}$, with the anatomical reference scans was performed for better lesion identification and analysis.

Dynamic modeling of the pyruvate to lactate conversion was calculated using a two-site exchange model including a pyruvate arterial input function (AIF) assumed to be a boxcar function, defined by injection rate $r_0$, similar to the model reported by Zierhut et al [19]. The model used is described in the following ODE form

$$dM_{pyr}(t)/dt = r_0 \cdot e^{-\rho t} \cdot [u(t) - u(t-a)] - (\rho + k_{PL})M_{pyr}(t) \quad (1)$$

$$dM_{lac}(t)/dt = k_{PL} \cdot M_{pyr}(t) - \rho \cdot M_{lac}(t) \quad (2)$$

where $M_x$ is the magnetization of metabolite x, and $k_{PL}$ is the pyruvate-to-lactate conversion rate constant. ρ is the relaxation coefficient, where $\rho = 1/T_1$, and *u(t)* is the unit step function, *a* is the bolus duration. Here the alanine fitting was included as it could improve the quantitative accuracy of $k_{PL}$.

The rate coefficient for pyruvate-to-lactate conversion, $k_{PL}$, was computed by applying the metabolic models to the in vivo HP-$^{13}C$ dynamic profile. The signal curves were fitted to the dynamic models using the non-linear least squares analysis. The mean was calculated over

the manually-selected tumor ROI for the $k_{PL}$ estimation, where only voxels with >85% tumor were incorporated. RF excitations and relaxation $T_1$ were included in the model to account for signal loss, where $T_1$ was assumed to be equal for all $^{13}C$ metabolites. The reverse conversion rate $k_{LP}$ was assumed to be zero in the model since it is much lower compared to the forward reaction in physiological conditions, and such assumption improves the stability of fitting computations [19, 20].

## 3. Results

### Preclinical studies

The acquisition was delayed by 15 seconds from the beginning of injection. Immediately following the arrival of HP-pyruvate in TRAMP tumor, lactate dehydrogenase (LDH) rapidly catalyzed the reduction reaction to HP-lactate. This reflected the upregulated LDH gene expression/activity in cancer as found previously [1]. Pyruvate signal displayed its maximum near the beginning of the acquisition, and then decreased due to the metabolic conversion, the RF excitation pulses and the $T_1$ relaxation. The lactate increased at the beginning of the sequence due to the rapid pyruvate-to-lactate conversion, reaching maximum at approximately t=14±4 seconds. The decreasing lobe at the latter half of the lactate curve indicated the timing where the combined loss from progressively increasing flip angle and $T_1$ relaxation exceeded the contribution from pyruvate conversion. Alanine was converted to a much lower degree from pyruvate as a key step in gluconeogenesis pathway, which is governed by the alanine transaminase. The alanine time curve approached maximum at t=20±6 seconds. The amount of alanine production was only a fraction of lactate in the TRAMP tumor, while higher alanine level can be seen in the liver of both cancerous and healthy animals [13].

In order to investigate the feasibility of imaging larger FOVs in vivo, we applied the 3D CS-EPSI sequence on 3 healthy rats. Rapid pyruvate perfusion/uptake into the kidney was observed since the beginning of the sequence, namely at around ~3 seconds after the end of the 12s-injection. Appreciable amount of lactate exchange was detected there as well (Fig. 3). Lactate and alanine production was also found in rat liver (data not shown). These outcomes were highly consistent with the previous observations on HP-$^{13}C$ rat studies [21, 22].

From TRAMP studies (Fig.4), the mean SNR, summed across time, of total carbon was 69.2±28.4 for tumor, 115.5±45.8 for vena cava, and 135.5±56.2 for kidneys with ~25–35% polarization on dissolution. In the rat scans (Fig.5), both FOV and voxel size were doubled from mice. High SNR was found in both rat kidney (172.5±100.3) and liver (85.7±50.1). Such SNR was adequate for both direct data visualization and dynamic modeling of metabolic interconversion. The mean size of TRAMP tumors, 2.2$cm^3$, was approximately equivalent to 37 voxels (voxel size = 0.059$cm^3$).

### Clinical Phantom Studies

Phantom studies were conducted using clinical setup, sequence and coils. The signal pattern on the built-in urea phantom was found to be of higher homogeneity compared to the

ethylene glycol phantoms (Fig.3). Such signal profile probably resulted from the reduced sensitivity in regions further away from the endorectal coil. The phantom data was acquired with our 3D CS-EPSI sequence in tandem with the new spectral-spatial RF pulses with reduced peak power and duration. On both pyruvate and lactate bands, the phantom dynamics showed good fitting agreement with the simulated signal profile (Fig.2B). The apparent SNR of ethylene glycol phantom was 16.1, and of urea phantom was 354 at the final timepoint, where the $^{13}C$ compounds were individually excited by the lactate excitation band with a mean flip angle ~40°.

## Patient Data

The subject of the human study testing the feasibility of the new 3D CS-EPSI methods was a 66 y/o male patient with biopsy-confirmed prostate cancer of stage T2c, with PSA level of 6ng/ml and PI-RADS score of 4/5. At radical prostatectomy (RP), bilateral Gleason 4+3 was found at the midgland of the prostate. Figure 6 depicts the pyruvate and lactate area under curve (AUC) overlays in the prostate region overlaid on T2w reference scan. It demonstrated full gland coverage of this new sequence, from apex to base, with a spatial resolution of 8×8×8mm isotropic (volumetric = 0.5cm$^3$). While pyruvate intensities encompass the prostate gland as well as some surrounding vasculatures, regions of elevated conversion to lactate correlated with cancer in the bilateral pathology data of this patient.

Figure 7 illustrates the temporal dynamics in a single slice containing bilateral prostate cancer confirmed at RP. HP-$^{13}C$ pyruvate is seen to perfuse into the vasculature surrounding the prostate, and the bolus entered prostate around ~t=10 seconds into the dynamic 3D acquisition. Rapid conversion to lactate in cancerous regions was observed to occur at ~t=20 seconds.

The biopsy-proven Gleason 4+3 tumor in the right peripheral zone exhibited more than 4-fold higher pyruvate-to-lactate conversion ($k_{PL}$) compared to normal-appearing regions, reflecting high LDH enzymatic activity. The tumor size was approximately 1.5 cm$^3$, or 3 voxels (voxel size = 0.5 cm$^3$). Figure 8C and D showed the HP-$^{13}C$ spectra and dynamics in a representative voxel of this tumor versus a normal-appearing region voxel. The dynamic curves were corrected for progressive flip angles to show the estimated HP magnetization for kinetic modeling visualization purposes. The raw signal of both pyruvate and lactate appears to monotonically increase until the end of acquisition (Fig.8B) due to the progressively increasing flip angles, while the corrected signal (i.e. the HP magnetization) shows the pyruvate maximizing near ~t=20 seconds post-injection and that of lactate around ~30 seconds and decrease toward the end (Fig.8C). The tumor region also corresponds to darker region in $T_2$-weighted FSE image (Fig.8A top, as encircled by the red box), and high intensity in high b-value ADC maps (Fig.8A bottom), both of which exhibited good consistency with biopsy and HP $^{13}C$ findings. The bilateral midgland Gleason 4+3 cancer found at radical prostatectomy was also consistent with the $k_{PL}$ map in Figure 8E, where the tumor in the right was larger than the one in the left.

In the right midgland cancer, the apparent SNR calculated for pyruvate was 104, and for lactate was 10.7 at the last timepoint. The mean SNR over the acquisition for pyruvate was 45.2, and was 6.1 for lactate. The mean SNR over all timepoints for total carbon was 51.3. In

normal-appearing regions, the mean SNR of total carbon in this patient was 48.2, comparable to the tumor region.

## 4. Discussion

Since HP $^{13}$C MR encodes chemical as well as spatial information, this new molecular imaging technique allows the simultaneous detection of multiple biologic compounds and metabolic products with sensitivity enhancements of >10,000 fold [23]. This technique therefore presents the fields of oncology and medical imaging with an opportunity to improve our ability to investigate human disease and to ultimately translate these techniques into the clinic for more individualized patient care.

The translation from animal to clinical HP-$^{13}$C imaging faces the challenges of larger imaging volume, reduced peak RF power and higher B1 inhomogeneity. To address these challenges, specialized sequence modifications were developed including a low-power spectral spatial RF excitation, “FID” acquisition mode and associated reconstruction methods, 3D coverage of the entire prostate with 0.5cm$^3$ spatial and 2-second temporal resolution for prostate cancer patient imaging. This study was designed to determine and test the sequence properties and signal behavior transitioning from mouse studies to rats and, then to a human subject, with the intent to optimize the performance and robustness of this new 3D dynamic acquisition approach and then determine its feasibility for imaging patients.

One major sequence modification made for the translation to human imaging was in the RF pulse design. The new spectral-spatial RF pulse provide 67% savings in peak B1 by means of relaxing the constraints on urea flip angle, which accounts for the reduced peak RF power from clamshell transmit coils in clinical setup compared to preclinical settings. The designed peak B1 was chosen to be around 60% the nominal maximum allowable power for the transmit coil in order to provide sufficient headroom in transmit power allow for varying coil loading when scanning different patients. The 1ppm (~30Hz) passband for each metabolite in this spectral-spatial pulse was reasonably wide to account for off-resonance, which is typically less than 0.2ppm (~6Hz) for TRAMP mice and less than 0.5ppm (~15Hz) for human prostate. The time-bandwidth of 5 provides good compromise between pulse duration, peak power and transition profile sharpness (Fig.2A). Also, the reduction in RF pulse width (8.9 to 6.3ms) shortened the echo time, which may slightly improve SNR given limited $T_2$ and $T_2$*. The phantom signal curve agrees well with the simulated signal profile, indicating that the excitation pulses can be confidently generated with the clinical coil configuration. Removing the DSE refocusing pulses also mitigated the issue of limited peak RF power. The mean SNR were comparable in TRAMP prostate tumor in the DSE-enabled sequence from prior studies and the new sequence in this study. (N=8, $SNR_{DSE}$ = 61.6±43.6, $SNR_{FID}$ = 69.2±28.4, P>0.3)

Imaging a larger subject using the 3D dynamic CS-EPSI acquisition protocol provided a way to investigate the sequence parameters and signal behavior due to increasing FOV. The rat scans in this study utilizes a dual-tuned rat coil which was about ~ 5 times the volume of mouse coil. The FOV and voxel size were doubled both in the phase encode and EPSI

readout direction (in-plane resolution: mouse 3.3mm and rat 6.7mm, axial resolution: mouse 5.4mm and rat 10.8mm), giving 4× voxel volume. The total injection dose also increased by approximately 6 fold. However, rat received lower HP-$^{13}$C dose per unit weight (around 60% that of TRAMP). In addition, the larger coil volumes inherently lead to decreased sensitivity compared to mouse setup. The other sequence parameters (e.g. flip angles, temporal resolution and undersampling ratio) remained the same. Substantial pyruvate and lactate were observed in rat kidneys just like in TRAMP mice tumors. Also, the SNR did not deteriorate in rat relative to mouse (Fig.4 and 5). As such, transitioning to rat scans revealed the key elements to scaling up the sequence, and this protocol showed robustness in signal and image quality with larger imaging subjects and coils.

A 2-second temporal resolution was chosen for human protocol, identical to that in TRAMP studies. In TRAMP scans, this consistently provided >30 (apparent) SNR for both pyruvate and lactate (~25–35% polarization), which translated into less than 3% error in quantitative metabolism models for $k_{PL}$ evaluation based on simulations. For the clinical study, the pyruvate SNR was similar to TRAMP (~30), while lactate SNR was relatively lower (~6). Two primary sources of uncertainty contribute to the apparent SNR of this 3D CS-EPSI acquisition, which are the data noise and CS reconstruction errors. Referring to Figure.3 of the paper by Larson et al.[15], the reconstruction error was less than 0.001 for SNR of 45, and less than 0.007 for SNR of 6. Therefore, it can be concluded that the data noise was dominant source of error under both clinical and mouse scheme. SNR improvement is theoretically possible through a longer temporal resolution, since it results in effective signal averaging and decrease of undersampling ratio. Nevertheless, a longer temporal resolution can create temporal blurring and ambiguity on timing of dynamic curve, which can negatively impact quantitative modeling.

In the patient research, the acquisition began at t=5 seconds post-injection, compared to the t=0 second in mouse studies, while both shared the same 2-second temporal resolution. The acquisition time window covered both bolus dynamics and pyruvate-to-lactate conversion in human prostate cancer, while the TRAMP scan focused more on the latter half of the pharmacokinetics that mainly reflected pyruvate metabolism. A main reason for the 5-second delay in human studies was to prevent hyperpolarized magnetization in the IV tubing and arm being excited by the clamshell transmit coils. Since at the end of the injection, the bolus could still be traversing through the antecubital vein, which is typically located inside the “hot” zones of the transmitter, the delay allows hyperpolarized bolus to perfuse into tumor region prior to RF excitation.

In clinical hyperpolarized $^{13}$C imaging, due to the absence of arterial coverage or perfusion markers, it is more challenging to account for pharmacokinetic parameters such as circulation and AIF. In contrast, since the bolus delivery was more rapid in small animals (e.g. TRAMP mice), and a reference AIF was relatively easy to estimate using the HP $^{13}$C urea through arterial voxels according to a preclinical co-polarized imaging study of TRAMP tumor [1], the sequence can be configured to put more focus on net metabolism by acquiring at a longer (15s) delayed window [1, 24]. Additionally, the circulation and bolus delivery is generally slower in human versus small animals. Therefore, carefully selecting an

acquisition window that both accounts for pyruvate infusion and pyruvate-lactate conversion benefits the clinical quantitation of prostate tumor metabolism.

Prostate cancer is a major health concern in the United States with >160,000 new cases per year and >26,000 deaths [25]. Due to increased screening using serum prostate specific antigen (PSA) and extended-template transrectal ultrasound (TRUS) guided biopsies, patients with prostate cancer are being identified at an earlier and potentially more treatable stage. Unfortunately, the aggressiveness of individual tumors cannot be predicted with great confidence in individual patients using currently available clinical and imaging prognostic data [26–30]. Preliminary data strongly indicate that hyperpolarized $^{13}$C-pyruvate MRI using DNP has the potential to dramatically improve prostate cancer clinical management. In transgenic prostate cancer mouse models, this method demonstrated the unprecedented ability to separate early stage (low-grade) tumors from late stage (high-grade) cancer based on this metabolic parameter (conversion through the LDH-catalyzed pyruvate metabolism) [2]. Higher grade prostate cancers, both in transgenic models and human biopsies, have demonstrated several fold increases in LDH expression [2, 31]. No other imaging method has demonstrated this ability to differentiate low grade, clinically insignificant prostate cancers which are the majority of cases from high-grade disease which kills >26,000 Americans per year. The Phase 1 clinical trial of HP $^{13}$C-pyruvate in prostate cancer patients demonstrated feasibility and safety through this first human study of hyperpolarized MR metabolic imaging [12] using single-slice 1D dynamic, 2D dynamic and 3D single timepoint acquisitions. This clinical trial indicated the potential to characterize the extent and aggressiveness of prostate cancer in individual subjects to ultimately benefit clinical treatment decisions and to monitor treatment response. However, the acquisition methods used in that trial did not provide simultaneously the required spatial and dynamic temporal resolution necessary for optimal HP $^{13}$C MR clinical research studies. Development and translation of 3D dynamic HP $^{13}$C MRSI offers a new method to quantitatively analyze metabolism in human prostate cancer throughout the gland. In this study, the human 3D MRSI acquisition demonstrated the ability to obtain dynamic information on the conversion of [1-$^{13}$C]pyruvate to [1-$^{13}$C]lactate that is catalyzed by lactate dehydrogenase (LDH) which is up-regulated in prostate cancer. Adequate SNR and temporal resolution enabled the calculation of $k_{PL}$ maps with a spatial resolution of 0.5cm$^3$. This supports the use of this 3D acquisition approach in future studies to investigate in sufficiently large patient populations prostate cancer aggressiveness and response to therapy. Also importantly, the capability to image biochemical processes and visualize diseases with high spatiotemporal resolution opens the door to many potential HP $^{13}$C translational and research applications. For instance, high lactate/pyruvate ratios were detected in various cancer types such as xenografts of human brain tumor [32], renal carcinoma cells [33], and breast tumor xenografts [7]. And modulation of lactate production were found in tumor subjected to chemo [34] and targeted therapy [35]. Besides cancer, HP $^{13}$C imaging has been used to study kidney urea transporters [36], diabetes and gluconeogenesis [37], cardiac diseases [38] and neurodevelopment [39].

## 5. Conclusions

This new 3D dynamic MRSI acquisition method incorporating new spectral-spatial RF pulses, “FID” readout and modified CS reconstruction addressed the challenges of larger imaging volumes, and reduced available peak RF power required for human studies. Scalability in acquisition, reconstruction and quantitation methods was demonstrated by the satisfactory image quality, SNR and apparent kinetic rate constants between cancer/normal during the transition from mice to human patient studies. The results demonstrate the feasibility to characterize prostate cancer metabolism in the clinical setting using this new 3D dynamic HP MR technique to quantify and image the kinetic rate constant, $k_{PL}$, of the conversion of [1-$^{13}$C]pyruvate to [1-$^{13}$C]lactate which has been shown to be increased in prostate cancer [1, 2, 12, 40, 41].

## Supplementary Material

Refer to Web version on PubMed Central for supplementary material.

## Acknowledgments

This work was supported by grants from the NIH (R01EB017449, R01EB013427, R01CA166655, and P41EB013598). We would also like to thank Dr. Renuka Sriram for the helpful discussions.

## References

1. Chen HY, Larson PEZ, Bok RA, von Morze C, Sriram R, Delos Santos R, et al. Assessing Prostate Cancer Aggressiveness with Hyperpolarized Dual-Agent 3D Dynamic Imaging of Metabolism and Perfusion. Cancer Res. 2017; 77(12):3207–16. [PubMed: 28428273]
2. Albers MJ, Bok R, Chen AP, Cunningham CH, Zierhut ML, Zhang VY, et al. Hyperpolarized 13C lactate, pyruvate, and alanine: noninvasive biomarkers for prostate cancer detection and grading. Cancer Res. 2008; 68(20):8607–15. [PubMed: 18922937]
3. Brindle K. New approaches for imaging tumour responses to treatment. Nat Rev Cancer. 2008; 8(2): 94–107. [PubMed: 18202697]
4. Day SE, Kettunen MI, Gallagher FA, Hu DE, Lerche M, Wolber J, et al. Detecting tumor response to treatment using hyperpolarized C-13 magnetic resonance imaging and spectroscopy (vol 13, pg 1382, 2007). Nat Med. 2007; 13(12):1521-.
5. Golman K, in 't Zandt R, Thaning M. Real-time metabolic imaging. Proc Natl Acad Sci U S A. 2006; 103(30):11270–5. [PubMed: 16837573]
6. Golman K, Olsson LE, Axelsson O, Mansson S, Karlsson M, Petersson J. Molecular imaging using hyperpolarized 13C. Br J Radiol. 2003; 76(suppl_2):S118–S27. [PubMed: 15572334]
7. Golman K, Zandt RI, Lerche M, Pehrson R, Ardenkjaer-Larsen JH. Metabolic imaging by hyperpolarized 13C magnetic resonance imaging for in vivo tumor diagnosis. Cancer Res. 2006; 66(22):10855–60. [PubMed: 17108122]
8. Ishii M, Emami K, Kadlecek S, Petersson JS, Golman K, Vahdat V, et al. Hyperpolarized 13C MRI of the pulmonary vasculature and parenchyma. Magn Reson Med. 2007; 57(3):459–63. [PubMed: 17326170]
9. Kurhanewicz J, Vigneron DB, Brindle K, Chekmenev EY, Comment A, Cunningham CH, et al. Analysis of cancer metabolism by imaging hyperpolarized nuclei: prospects for translation to clinical research. Neoplasia. 2011; 13(2):81–97. [PubMed: 21403835]
10. Merritt ME, Harrison C, Storey C, Jeffrey FM, Sherry AD, Malloy CR. Hyperpolarized C-13 allows a direct measure of flux through a single enzyme-catalyzed step by NMR. Proc Natl Acad Sci U S A. 2007; 104(50):19773–7. [PubMed: 18056642]

11. Nelson SJ, Vigneron D, Kurhanewicz J, Chen A, Bok R, Hurd R. DNP-hyperpolarized C-13 magnetic resonance metabolic imaging for cancer applications. Appl Magn Reson. 2008; 34(3–4): 533–44. [PubMed: 20198109]
12. Nelson SJ, Kurhanewicz J, Vigneron DB, Larson PEZ, Harzstark AL, Ferrone M, et al. Metabolic Imaging of Patients with Prostate Cancer Using Hyperpolarized [1-C-13]Pyruvate. Sci Transl Med. 2013; 5(198)
13. Chen AP, Albers MJ, Cunningham CH, Kohler SJ, Yen YF, Hurd RE, et al. Hyperpolarized c-13 spectroscopic imaging of the TRAMP mouse at 3T - Initial experience. Magn Reson Med. 2007; 58(6):1099–106. [PubMed: 17969006]
14. Hu S, Lustig M, Balakrishnan A, Larson PEZ, Bok R, Kurhanewicz J, et al. 3D Compressed Sensing for Highly Accelerated Hyperpolarized C-13 MRSI With In Vivo Applications to Transgenic Mouse Models of Cancer. Magnet Reson Med. 2010; 63(2):312–21.
15. Larson PEZ, Hu S, Lustig M, Kerr AB, Nelson SJ, Kurhanewicz J, et al. Fast Dynamic 3D MR Spectroscopic Imaging With Compressed Sensing and Multiband Excitation Pulses for Hyperpolarized C-13 Studies. Magn Reson Med. 2011; 65(3):610–9. [PubMed: 20939089]
16. Xing Y, Reed GD, Pauly JM, Kerr AB, Larson PEZ. Optimal variable flip angle schemes for dynamic acquisition of exchanging hyperpolarized substrates. J Magn Reson. 2013; 234:75–81. [PubMed: 23845910]
17. Larson PEZ, Bok R, Kerr AB, Lustig M, Hu S, Chen AP, et al. Investigation of Tumor Hyperpolarized [1-C-13]-Pyruvate Dynamics Using Time-Resolved Multiband RF Excitation Echo-Planar MRSI. Magn Reson Med. 2010; 63(3):582–91. [PubMed: 20187172]
18. Crane JC, Olson MP, Nelson SJ. SIVIC: Open-Source, Standards-Based Software for DICOM MR Spectroscopy Workflows. Int J Biomed Imaging. 2013; 2013:169526. [PubMed: 23970895]
19. Zierhut ML, Yen YF, Chen AP, Bok R, Albers MJ, Zhang V, et al. Kinetic modeling of hyperpolarized 13C1-pyruvate metabolism in normal rats and TRAMP mice. J Magn Reson. 2010; 202(1):85–92. [PubMed: 19884027]
20. Bahrami N, Swisher CL, Von Morze C, Vigneron DB, Larson PE. Kinetic and perfusion modeling of hyperpolarized (13)C pyruvate and urea in cancer with arbitrary RF flip angles. Quant Imaging Med Surg. 2014; 4(1):24–32. [PubMed: 24649432]
21. Hu S, Larson PEZ, VanCriekinge M, Leach AM, Park I, Leon C, et al. Rapid sequential injections of hyperpolarized [1-C-13]pyruvate in vivo using a sub-kelvin, multi-sample DNP polarizer. Magn Reson Imaging. 2013; 31(4):490–6. [PubMed: 23107275]
22. Kohler SJ, Yen Y, Wolber J, Chen AP, Albers MJ, Bok R, et al. In vivo (13)carbon metabolic imaging at 3T with hyperpolarized C-13-1-pyruvate. Magn Reson Med. 2007; 58(1):65–9. [PubMed: 17659629]
23. Ardenkjaer-Larsen JH, Fridlund B, Gram A, Hansson G, Hansson L, Lerche MH, et al. Increase in signal-to-noise ratio of >10,000 times in liquid-state NMR. Proc Natl Acad Sci U S A. 2003; 100(18):10158–63. [PubMed: 12930897]
24. von Morze C, Larson PEZ, Hu S, Keshari K, Wilson DM, Ardenkjaer-Larsen JH, et al. Imaging of Blood Flow Using Hyperpolarized [C-13] Urea in Preclinical Cancer Models. J Magn Reson Imaging. 2011; 33(3):692–7. [PubMed: 21563254]
25. Society AC. Cancer Facts & Figures 2017. American Cancer Society. 2017
26. Bill-Axelson A, Holmberg L, Ruutu M, Haggman M, Andersson SO, Bratell S, et al. Radical prostatectomy versus watchful waiting in early prostate cancer. New Engl J Med. 2005; 352(19): 1977–84. [PubMed: 15888698]
27. Carroll PR. Early stage prostate cancer - Do we have a problem with over-detection, overtreatment or both? J Urol. 2005; 173(4):1061–2. [PubMed: 15758699]
28. Draisma G, Boer R, Otto SJ, van der Cruijsen IW, Damhuis RAM, Schroder FH, et al. Lead times and overdetection due to prostate-specific antigen screening: Estimates from the European randomized study of screening for prostate cancer. J Natl Cancer Inst. 2003; 95(12):868–78. [PubMed: 12813170]
29. Etzioni R, Penson DF, Legler JM, Di Tommaso D, Boer R, Gann PH, et al. Overdiagnosis due to prostate-specific antigen screening: lessons from US prostate cancer incidence trends. J Natl Cancer I. 2002; 94(13):981–90.

30. Johansson JE, Andren O, Andersson SO, Dickman PW, Holmberg L, Magnuson A, et al. Natural history of early, localized prostate cancer. Jama-J Am Med Assoc. 2004; 291(22):2713–9.

31. Tessem MB, Swanson MG, Keshari KR, Albers MJ, Joun D, Tabatabai ZL, et al. Evaluation of lactate and alanine as metabolic biomarkers of prostate cancer using H-1 HR-MAS spectroscopy of biopsy tissues. Magn Reson Med. 2008; 60(3):510–6. [PubMed: 18727052]

32. Park I, Larson PEZ, Zierhut ML, Hu S, Bok R, Ozawa T, et al. Hyperpolarized C-13 magnetic resonance metabolic imaging: application to brain tumors. Neuro Oncol. 2010; 12(2):133–44. [PubMed: 20150380]

33. Keshari KR, Sriram R, Van Criekinge M, Wilson DM, Wang ZJ, Vigneron DB, et al. Metabolic reprogramming and validation of hyperpolarized 13C lactate as a prostate cancer biomarker using a human prostate tissue slice culture bioreactor. Prostate. 2013; 73(11):1171–81. [PubMed: 23532911]

34. Park I, Bok R, Ozawa T, Phillips JJ, James CD, Vigneron DB, et al. Detection of early response to temozolomide treatment in brain tumors using hyperpolarized 13C MR metabolic imaging. J Magn Reson Imaging. 2011; 33(6):1284–90. [PubMed: 21590996]

35. Lodi A, Woods SM, Ronen SM. Treatment with the MEK inhibitor U0126 induces decreased hyperpolarized pyruvate to lactate conversion in breast, but not prostate, cancer cells. NMR Biomed. 2013; 26(3):299–306. [PubMed: 22945392]

36. von Morze C, Larson PEZ, Hu S, Keshari K, Wilson DM, Ardenkjaer-Larsen JH, et al. Imaging of blood flow using hyperpolarized [13C]Urea in preclinical cancer models. J Magn Reson Imaging. 2011; 33(3):692–7. [PubMed: 21563254]

37. Hu S, Chen AP, Zierhut ML, Bok R, Yen YF, Schroeder MA, et al. In Vivo Carbon-13 Dynamic MRS and MRSI of Normal and Fasted Rat Liver with Hyperpolarized C-13-Pyruvate. Mol Imag Biol. 2009; 11(6):399–407.

38. Schroeder MA, Lau AZ, Chen AP, Gu Y, Nagendran J, Barry J, et al. Hyperpolarized (13)C magnetic resonance reveals early- and late-onset changes to in vivo pyruvate metabolism in the failing heart. Eur J Heart Fail. 2013; 15(2):130–40. [PubMed: 23258802]

39. Chen YR, Kim H, Bok R, Sukumar S, Mu X, Sheldon RA, et al. Pyruvate to Lactate Metabolic Changes during Neurodevelopment Measured Dynamically Using Hyperpolarized C-13 Imaging in Juvenile Murine Brain. Dev Neurosci. 2016; 38(1):34–40. [PubMed: 26550989]

40. Keshari KR, Sriram R, Van Criekinge M, Wilson DM, Wang ZJ, Vigneron DB, et al. Metabolic Reprogramming and Validation of Hyperpolarized C-13 Lactate as a Prostate Cancer Biomarker Using a Human Prostate Tissue Slice Culture Bioreactor. Prostate. 2013; 73(11):1171–81. [PubMed: 23532911]

41. Wilson DM, Kurhanewicz J. Hyperpolarized 13C MR for molecular imaging of prostate cancer. J Nucl Med. 2014; 55(10):1567–72. [PubMed: 25168625]

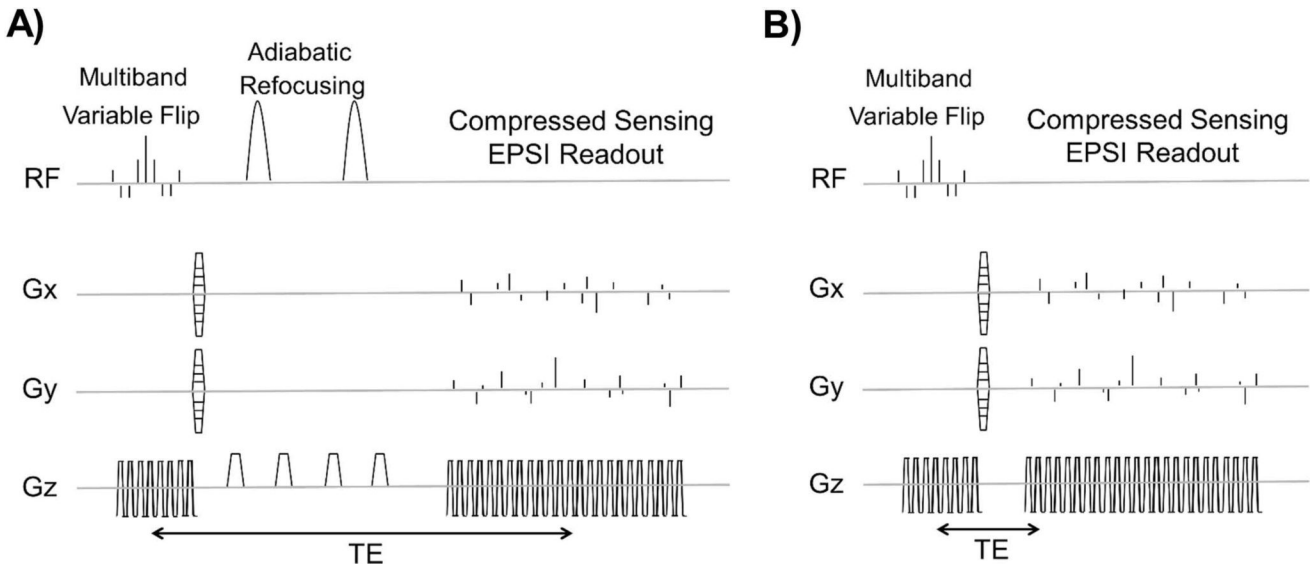


**Figure 1.**

The HP-$^{13}$C 3D CS-EPSI sequence diagram designed for in vivo studies. **A)** The double spin-echo enabled (DSE mode) was utilized in a previous report of mouse prostate cancer imaging [1]. **B)** The imaging mode (FID mode) in this study was chosen for larger imaging volumes and to account for peak B1 limitations with the human coil setup.

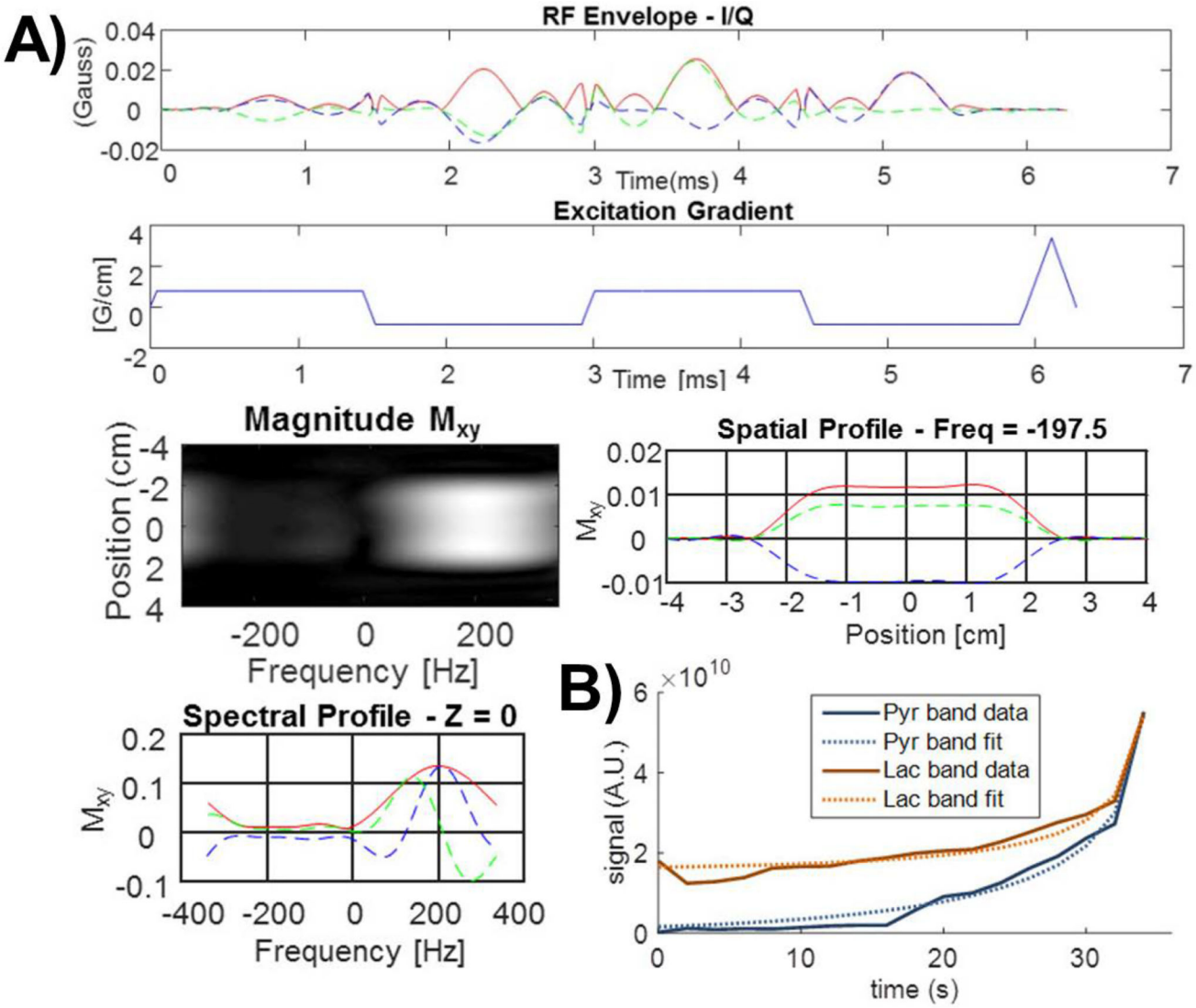


**Figure 2.**

New spectral-spatial RF pulses were designed using the ss-RF toolbox by Larson et al. [17] **A)** The 6.3ms-long RF pulse excites $^{13}$C pyruvate and lactate with independent variable flip angles. (Red is magnitude, blue is real, and green is imaginary components.) The peak B1 of 0.597G is a 67% reduction from that used for preclinical studies **B)** Phantom data excited with progressive-increasing flip RF showed good agreement with simulated profile.

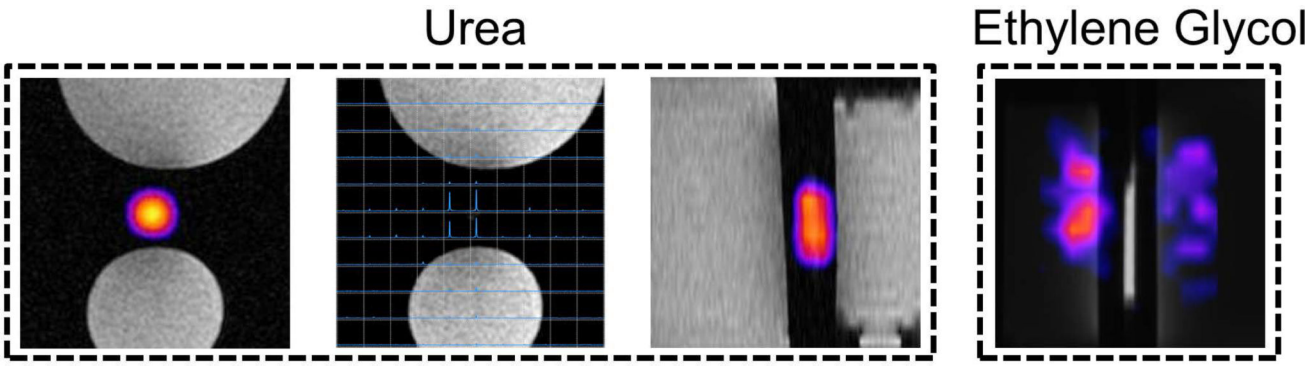


**Figure 3.**
Phantom studies using the clinical setup, the 3D CS-EPSI sequence and the new RF pulses showed good spatial homogeneity in a urea syringe.

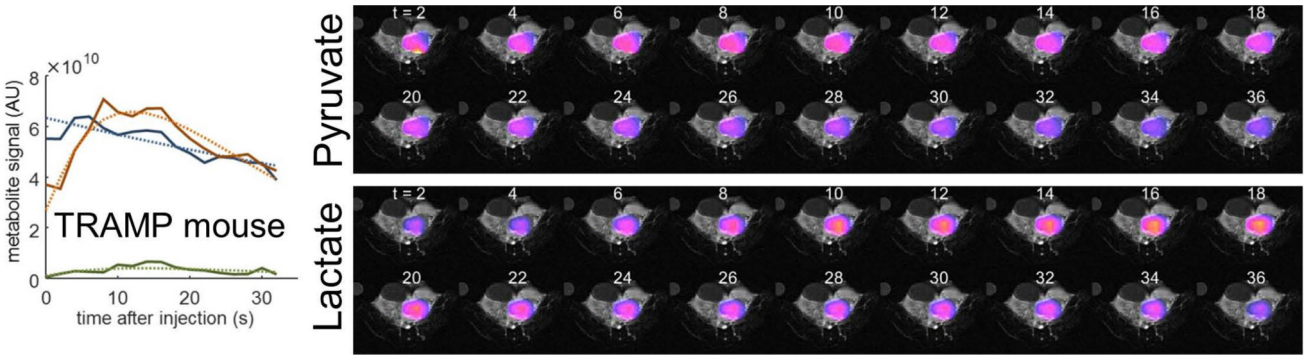


**Figure 4.**

Similar to the "DSE" mode, the in-vivo dynamics of $^{13}C$ biomarker acquired using the 3D dynamic CS-EPSI "FID" mode can be quantitatively analyzed by compartmental exchange models. Pyruvate and lactate dynamics were overlaid on T2-FSE scan in a low-grade TRAMP tumor. The calculated $k_{PL}$ value was 0.0297($s^{-1}$).

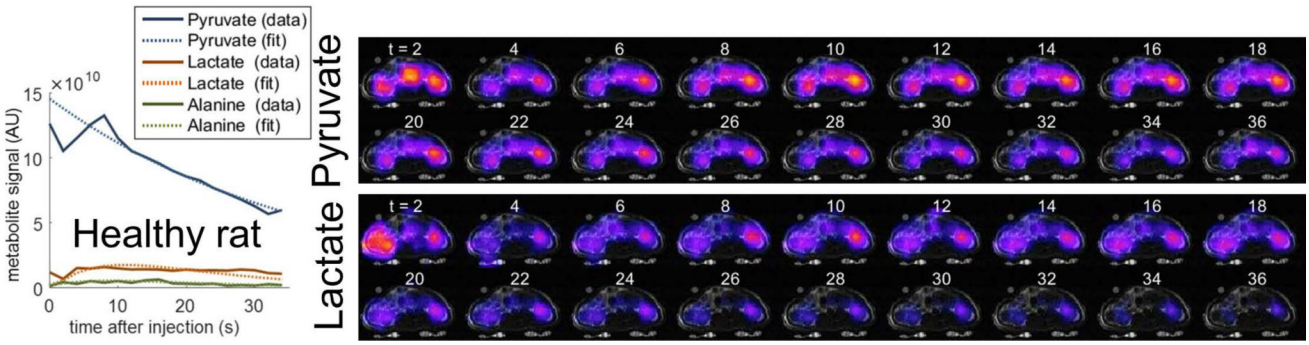


**Figure 5.**

Pyruvate to lactate conversion in the kidneys of healthy rat is visualized in this $^{13}C$ image overlaid on bSSFP reference. The calculated $k_{PL}$ was 0.0058($s^{-1}$).

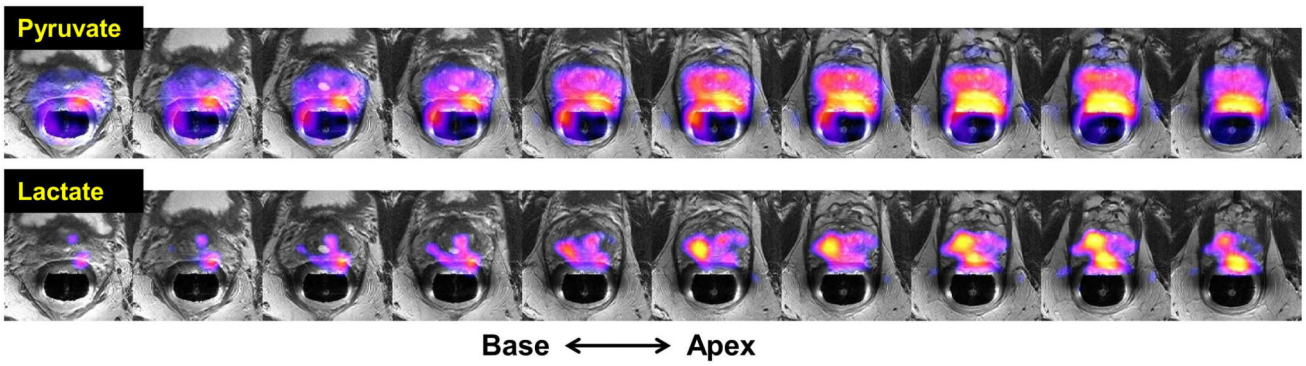


**Figure 6.**

Prostate cancer patient 3D dynamic CS-EPSI data with volumetric coverage from base to apex of HP pyruvate and its conversion to lactate (signal summed through time is shown in the overlays). Spatial resolution=0.5cm$^3$, temporal=2s, 18 timepoints, starting 5s after injection of HP (37%) [1-$^{13}$C]pyruvate. Region of high lactate conversion correlated with the bilateral biopsy-confirmed cancer.

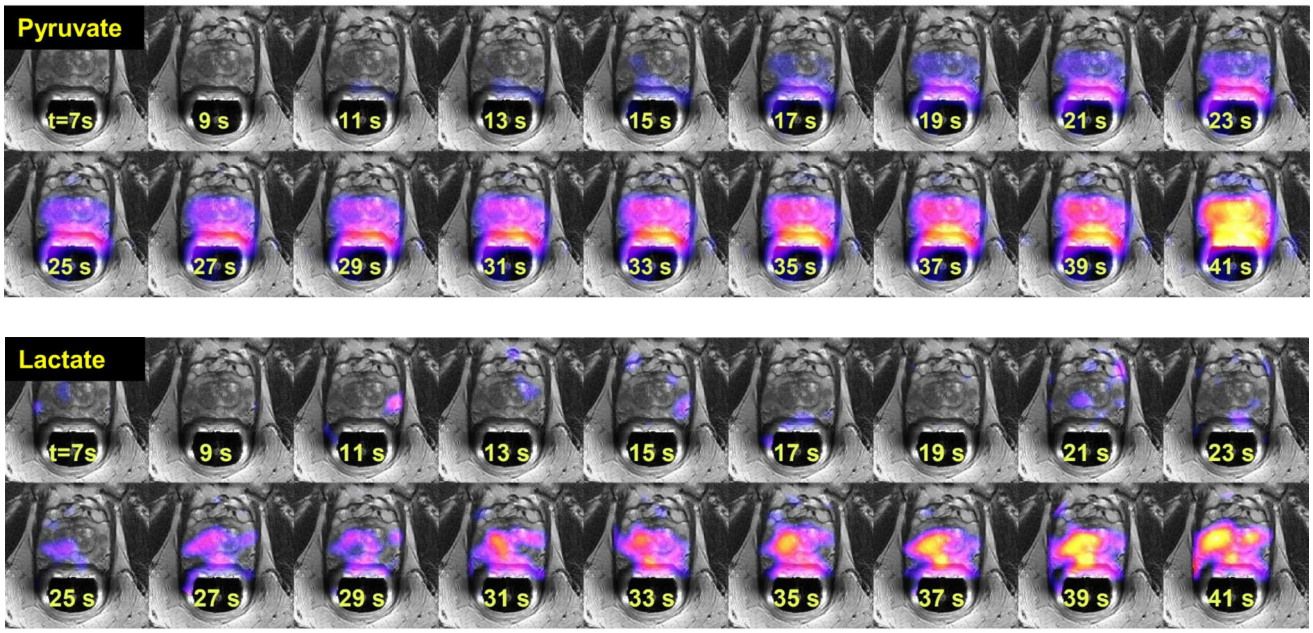


**Figure 7.**

**A)** 18 timepoints for HP $^{13}$C-pyruvate from a single slice with bilateral biopsy-confirmed prostate cancer. The acquisition began ~5s after injection. HP-$^{13}$C pyruvate appears in the prostate at ~10s into the dynamic 3D CS-EPSI acquisition. This data demonstrates the feasibility of acquiring dynamically in three-dimensions that covered the entire prostate with 2s temporal resolution. **B)** Temporal dynamics of $^{13}$C-lactate from the same data and slice as in A. Conversion to lactate in the bilateral cancer regions was observed at ~20 seconds.

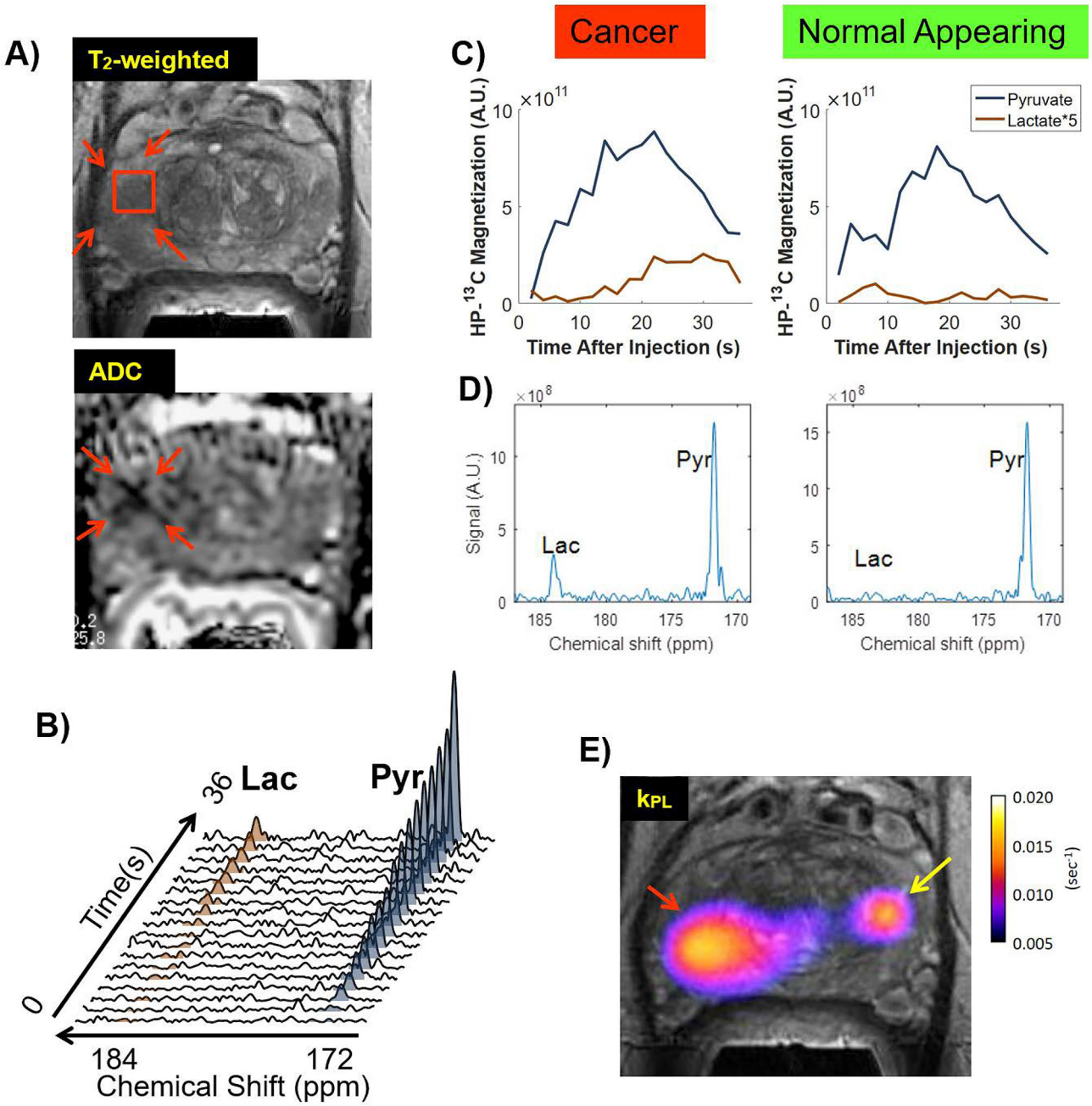


**Figure 8.**

The biopsy-proven Gleason 4+3 tumor in the patient's right lateral midgland (red arrow) exhibited high lactate conversion following HP pyruvate injection. **A)** T2-FSE image showing the tumor voxel selected for the dynamic spectral plot in **B)**. Also shown is the ADC map where the tumor region has substantially reduced ADC. **C)** Dynamic curves (corrected for variable flip angle) are shown with far higher conversion to lactate in cancer compared to normal appearing regions. **D)** Representative spectra for these regions at t=36 s. **E)** Pyruvate-to-lactate conversion rate $k_{PL}$ parameter map overlays showed high $k_{PL}$ on the

opposite side (yellow arrows) as well, which was also confirmed as Gleason 4+3 prostate cancer by post-surgical histopathology.